

# Silicon-Photonics Point Sensor for High-Resolution Optoacoustic Imaging

Rami Shnaiderman,\* Qutaiba Mustafa, Okan Ülgen, Georg Wissmeyer, Héctor Estrada, Daniel Razansky, Andriy Chmyrov, and Vasilis Ntziachristos\*

The recent development of ultrasound sensing using the silicon-photonics platform has enabled super-resolution optoacoustic imaging not possible by piezoelectric technology or polymeric optical microresonators. The silicon waveguide etalon detector (SWED) design exploits the sub-micrometer light confinement in the cross-section of a silicon strip waveguide to achieve a sensor aperture which is 13-fold to 30-fold smaller than the cutoff wavelength of the sensor. While its performance in near-field scanning optoacoustic imaging has been previously studied, the operational characteristics of this sensor as it relates to conventional optoacoustic imaging applications are not known. Here, for the first time, the application of the SWED in optoacoustic mesoscopy is investigated, the interaction of the sensor with ultrasound in the far-field is characterized, the acoustic point spread function up to a depth of 10 mm is measured, and 3D vasculature-mimicking phantoms are imaged. The measured point spread function of the sensor shows that surface acoustic waves can degrade the lateral resolution. Nevertheless, superior resolution is demonstrated over any state-of-the-art ultrasound sensor, over the whole range of imaging depths that are of interest to optoacoustic mesoscopy. Silicon photonics is proposed as a powerful and promising new platform for ultrasonics and optoacoustics.

## 1. Introduction

Optical detection has a fundamental advantage over piezoelectric detection in optoacoustic imaging, because sensors can be miniaturized without sacrificing sensitivity.<sup>[1]</sup> Smaller sensing elements lead to wider bandwidths and acceptance angles, which are essential components for increasing image resolution.<sup>[2]</sup> Current state-of-the-art piezoelectric sensor arrays employed in medical ultrasound and optoacoustic imaging offer resolutions of several hundreds of micrometers<sup>[3]</sup> which may not be sufficient for observations at the cellular level.<sup>[4,5]</sup> However, miniaturization comes at the cost of steep sensitivity loss, as the sensitivity of piezoelectric elements drops quadratically with element size. The resolution can be improved to several tens of micrometers by using acoustic lenses,<sup>[6]</sup> but at added manufacturing costs and complexity. In addition, the large element size makes this configuration unattractive for manufacturing of arrays as it would result in a pitch that is

much larger than the acoustic wavelength, strongly degrading the lateral resolution due to undersampling.

Optical microfabricated resonators are emerging as a promising alternative to piezoelectric elements, especially for optoacoustic imaging applications. In optoacoustic mesoscopy, the ultrasonic signals are excited by illuminating the sample with a pulsed laser. The light is unfocused and diffused and the resolution is therefore determined by the acoustic wavelength ( $\lambda_s$ ) and the sensor characteristics<sup>[2]</sup>

$$R_A \approx 0.8v_s/f_{\text{cut}} \quad (1)$$

$$R_L = [(R_A)^2 + (\phi_d)^2]^{1/2} \quad (2)$$


where  $R_A$  is the axial resolution,  $R_L$  is the lateral resolution,  $v_s$  is the speed of sound,  $f_{\text{cut}}$  is the cutoff frequency of the sensor, and  $\phi_d$  is the aperture of the sensor. Equation (2) shows that isometric resolution is possible only when the sensor aperture is smaller than the acoustic wavelength  $\phi_d \ll 0.8v_s/f_{\text{cut}}$ ; to fulfill this condition, a point sensor is required.

Optical resonators can be manufactured in small sizes leading to resolution improvements over piezoelectric elements, even when the latter employ acoustic lenses. The small

Dr. R. Shnaiderman, Q. Mustafa, O. Ülgen, Dr. G. Wissmeyer, Dr. H. Estrada, Prof. D. Razansky, Dr. A. Chmyrov, Prof. V. Ntziachristos  
Chair of Biological Imaging  
Center for Translational Cancer Research (TranslaTUM)  
School of Medicine  
Technical University of Munich  
D-81675 Munich, Germany  
E-mail: rami.shnaiderman@tum.de; v.ntziachristos@tum.de

Dr. R. Shnaiderman, Q. Mustafa, O. Ülgen, Dr. G. Wissmeyer, Dr. H. Estrada, Prof. D. Razansky, Dr. A. Chmyrov, Prof. V. Ntziachristos  
Institute of Biological and Medical Imaging  
Helmholtz Zentrum München (GmbH)  
D-85764 Neuherberg, Germany

Dr. H. Estrada, Prof. D. Razansky  
Institute for Biomedical Engineering  
University of Zurich and ETH Zurich  
Zurich CH-8093, Switzerland

 The ORCID identification number(s) for the author(s) of this article can be found under <https://doi.org/10.1002/adom.202100256>.

© 2021 The Authors. Advanced Optical Materials published by Wiley-VCH GmbH. This is an open access article under the terms of the Creative Commons Attribution License, which permits use, distribution and reproduction in any medium, provided the original work is properly cited.

DOI: 10.1002/adom.202100256

size further leads to high-detection bandwidth and sensitivity which is decoupled from the sensor aperture. A prominent example is the polymer microring resonator (MRR) fabricated with imprint technology. Such sensors have been demonstrated with diameters as small as 60  $\mu\text{m}$  and bandwidths above 300 MHz.<sup>[7]</sup> Their optical transparency and small sizes offer easy integration into existing microscopy systems<sup>[8]</sup> and endoscopes.<sup>[9]</sup> Optical resonators detect ultrasound waves based on resonance wavelength shifts occurring in response to ultrasound-induced changes in cavity length and the photoelastic effect. The shifts modulate the transmitted or reflected intensity from the modulator, and the amplitude of the modulations is proportional to the  $Q$ -factor of the resonator.<sup>[10]</sup> The high sensitivity of MRRs can be attributed to the large photoelastic coefficients and the low Young's modulus of the polymer. At the same time, the weak refractive index contrast  $\Delta n < 0.5$  between the polymer resonator and its cladding negates further miniaturization due to poor light confinement and bending losses.<sup>[7]</sup>

We have recently proposed the silicon-photonics platform for further improving the ultrasound detection performance of optical microresonators.<sup>[11]</sup> We demonstrated the silicon waveguide etalon detector (SWED) manufactured using CMOS compatible processes on a silicon-on-insulator (SOI) wafer. The SOI wafer offers a particularly high index contrast ( $\Delta n \approx 2.5$ ) between the silicon resonator and the silica cladding which enables efficient light confinement in sub-micrometer dimensions. In addition, silicon photonics offers high scalability and can incorporate a large variety of passive and active optical components, manufactured by high-throughput fabrication techniques widely used in the semiconductor industry.<sup>[12]</sup> We found<sup>[11]</sup> that the SWED has a noise equivalent pressure of 9 mPa Hz<sup>-1/2</sup>, which is 3 orders of magnitude more sensitive than the MRR when normalized by the aperture, and a wide detection bandwidth of 230 MHz. In analogy to near-field scanning optical microscopy, we utilized the subwavelength aperture of the SWED ( $220 \times 500 \text{ nm}^2$ ) to achieve  $50/\lambda_s$  super-resolution optoacoustic imaging at imaging depth  $< \lambda_s$ . We also demonstrated that at imaging depth  $> \lambda_s$ , the resolution degrades due to diffraction of the acoustic waves. However, the performance of this sensor in mesoscopic optoacoustic imaging by resolving depths in the millimeter range is not yet known.

In this work, we investigated the far-field ( $> \lambda_s$ ) operational characteristics of the SWED when employed in mesoscopy applications. In particular, we studied whether the sensor could be also beneficial in conventional optoacoustic imaging. Far-field operation has clinical relevance, since optoacoustic mesoscopy is already utilized in animal and clinical applications.<sup>[4,13,14]</sup> To explore these characteristics, we measured the acoustic point spread function (PSF) of the SWED up to a depth of 10 mm and imaged 3D vasculature-mimicking phantoms. We show that ultrasound can interact with the silicon-photonics platform in two prominent ways: direct detection of longitudinal waves (L-waves) and indirect detection through conversion of L-waves to surface acoustic waves (SAWs). We analyzed the response of the SWED to each of the wave types and their contribution to image formation. SAWs are demonstrated to degrade the lateral resolution by introducing artefacts to the images. We demonstrate enhanced lateral and axial resolutions compared to state-of-the-art sensors, yielding a twofold and sixfold

improvement compared to piezoelectric focused sensors commonly employed in optoacoustic mesoscopy, and outline ways for further improving on those figures. These results, together with the possibility of dense array manufacturing, position the silicon-photonics platform as an exciting alternative that can drive new developments in the fields of ultrasonic and optoacoustic imaging.

## 2. Sensor Design and Experimental Setup

The working principle of the SWED and the characterization system are shown in **Figure 1a**. The sensor is based on a silicon waveguide Bragg grating with a cross-section of  $220 \times 500 \text{ nm}^2$ , side-wall corrugation of  $\Delta w = 40 \text{ nm}$ , and a period of  $\Lambda = 320 \text{ nm}$ , fabricated on top of a SOI chip of  $3 \times 3 \text{ mm}^2$ . **Figure 1b** depicts the cross-section of the chip which consists of 800  $\mu\text{m}$  of silicon substrate, 1.5  $\mu\text{m}$  of silica known as back-oxide layer ("BOX," **Figure 1b**) which is the bottom cladding of the waveguide, 220 nm of silicon layer used for the fabrication of the photonics devices, and  $\approx 1.35 \mu\text{m}$  of silica known as top-oxide ("TOX," **Figure 1b**) which is the top cladding of the waveguide. Prior to the deposition of the TOX layer, the photonic devices are fabricated in the device layer using ultraviolet lithography and etch process of the silicon. The resonator is formed by inserting a discontinuity of  $L_{\text{cavity}} = 320 \text{ nm}$  in the Bragg periodicity to form an optical cavity, dividing the grating into a shorter "spacer" section with  $L_{\text{spacer}} \approx 9 \mu\text{m}$  and the longer "Bragg" section with  $L_{\text{Bragg}} = 125 \mu\text{m}$ .

The etalon is located close to the edge of the chip with  $L_{\text{spacer}}$  defining the distance between the optical cavity and the chip's facet (**Figure 1a**). Short spacer length is desirable in order to increase the sensitivity of the sensor by exposing more of the confined optical field in the cavity to ultrasound.  $L_{\text{spacer}}$  of 9  $\mu\text{m}$  was demonstrated before to achieve the highest detection bandwidth, which results in the highest  $f_{\text{cut}}$ ,<sup>[11]</sup> therefore it was selected in order to increase the imaging resolution (Equations (1) and (2)). The reduced reflectivity of the spacer section is compensated by sputtering an  $\approx 200 \text{ nm}$  gold layer on the chip facet, which equalizes the reflectivity of the spacer and Bragg sections and ensures large  $Q$ -factors. In addition, the gold layer masks the optical mode (**Figure 1c**) from the surroundings and prevents optical losses. At the same time, the layer is sufficiently thin to prevent blocking of ultrasound waves or adding an acoustic impedance mismatch.

We manufactured an array of 8 SWEDs. Each of the SWEDs in the array is connected to an  $\approx 2 \text{ mm}$  long silicon waveguide terminating at a fiber grating coupler. The grating couplers form an array with a pitch of 127  $\mu\text{m}$  which acts as an interface between the SWEDs and an array of single-mode polarization-maintaining fibers with identical pitch. In order to maximize the transmission efficiency, the facet of the fiber array is polished so the light is incident on the grating couplers with an angle of  $7^\circ$  relative to the normal to the chip surface, and the fibers are oriented to excite the transverse electric (TE) mode in the silicon waveguide.<sup>[15]</sup> The fiber array is attached to the chip using a ultraviolet-curable epoxy transparent in the C-band.

**Figure 1c** shows a brightfield microscopy image of the SWED array taken when the microscope camera was in parallel

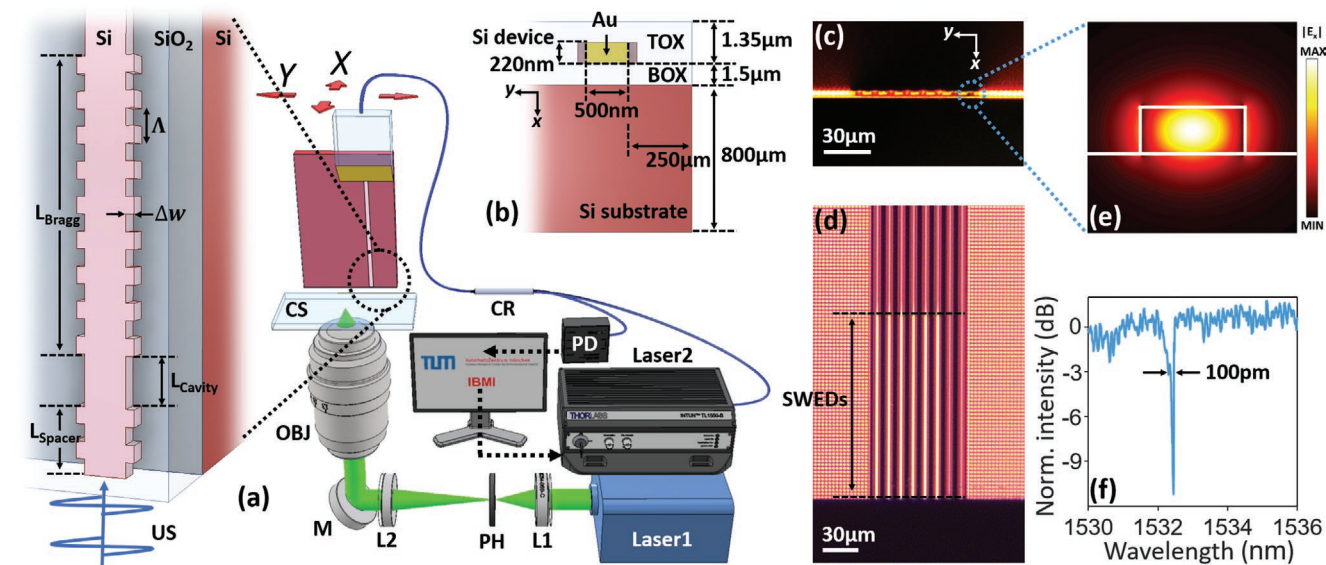


**Figure 1.** The silicon waveguide etalon detector (SWED) and the imaging system. a) Principle of operation of the SWED and the imaging system. CR, fiber circulator; CS, coverslip; OBJ, microscope objective; M, mirror; L (1, 2), lenses; M, mirror; PH, pinhole; PD photodiode; Laser1, 532 nm excitation pulsed laser; Laser2, infrared tunable CW laser; US, ultrasound. b) A cross-sectional view of the waver and the SWED. c) Brightfield microscopy image of the SWED array taken when the microscope camera is parallel to the apertures of the SWEDs. d) Brightfield microscopy image of the SWED array taken when the microscope camera is parallel to the waveguide Bragg gratings. e) Simulated profile of the optical field ( $E_x$ ) in the cross-section of the SWED of the TE mode. f) Optical spectrum reflected from the SWED.

to the apertures of the SWEDs, and Figure 1d shows a bright-field microscopy image taken when the microscope camera was in parallel to the waveguide Bragg gratings. The pitch of the SWED array was chosen to be 10 μm, an arbitrary choice which can be safely reduced to few micrometers. Figure 1e shows the simulated profile of the optical field in the cross-section of the SWED. The excited TE mode is strongly confined to the cross-section of the silicon waveguide, ensuring ultrasound detection is limited to within this area, and no cross talk between the SWEDs is possible even if the pitch is greatly reduced. The dimensions of the SWEDs were chosen to produce a single resonance in the widely utilized near-infrared C-band (Figure 1d) because the low propagation losses of silicon in this band give rise to a large  $Q$ -factor of  $1.5 \times 10^4$ .

For ultrasound detection, a tunable continuous wave (CW) laser ("Laser2," Figure 1a) pumps light through the fiber to the SWED. The pump wavelength is tuned off-resonance to the point of maximum slope, ensuring maximum amplification of the phase variations in response to incident ultrasound waves ("US"; Figure 1a). The reflected intensity modulations are routed by the fiber circulator ("CR"; Figure 1a) to the photodiode ("PD"; Figure 1a) and recorded by a digitizer with a sampling rate of 3 Gs  $s^{-1}$ .

Ultrasonic waves were excited using a 532 nm pulsed laser with pulse width of 1.2 ns and repetition rate of 1.2 kHz ("Laser1"; Figure 1a). For the characterization experiments, the laser beam was guided through a 25 μm pinhole for spatial filtering ("PH"; Figure 1a) and resized in a telescope ("L1" and "L2"; Figure 1a) and then focused with a 10× magnification and numerical aperture (NA) of 0.25 microscope objective ("OBJ"; Figure 1a) onto a microscope cover slip holding the sample ("CS"; Figure 1a). For the imaging experiments, ultrasonic signals were excited

by illuminating the phantoms with unfocused light emitted from a multimode fiber with 200 μm core and NA = 0.22 (not shown in Figure 1a) coupled to the excitation laser ("Laser 1"; Figure 1a). The fiber was aligned with the SWED to perform epi-illumination imaging, producing a spot of ≈2 mm on the cover slip under the SWED. All the images were reconstructed using a back-projection method in Fourier space.<sup>[16]</sup>

### 3. Interaction of Ultrasound with the Sensor and Resolution Characterization

To study the interaction of the SWED with ultrasound and how it effects image quality, we characterized the sensor's acoustic PSF. The SWED was mounted onto 2D linear translation stages and scanned along 4 mm (10 μm step) at a distance of 530 μm over an acoustic broadband point source. The point source was generated by sputtering the cover slip with gold film ≈200 nm thick<sup>[17]</sup> and acoustically coupling it to the SWED with a few drops of water.

Linear scans of the SWED (B-scans) along the  $x$ - and  $y$ -axes are depicted in Figure 2a,d, respectively. At each coordinate, the ultrasonic signals were recorded as a function of time with 300 averages and a [2, 350] MHz band-pass filter. Both of the B-scans show curved profiles, indicating direct propagation of L-waves in water from the source to the aperture of the SWED ("L-wave," Figure 2a,d). The shape of these profiles correspond to  $r(t) = \sqrt{(v_s t)^2 - h^2}$ , where  $r$  is the scanning distance in the  $xy$ -plane from (0,0),  $v_s$  is the speed of sound,  $t$  is the time, and  $h$  is the distance of the chip from the cover slip.

By fitting these profiles, we found that the signals arrive with a velocity of ≈1500 m  $s^{-1}$  which corresponds to the speed



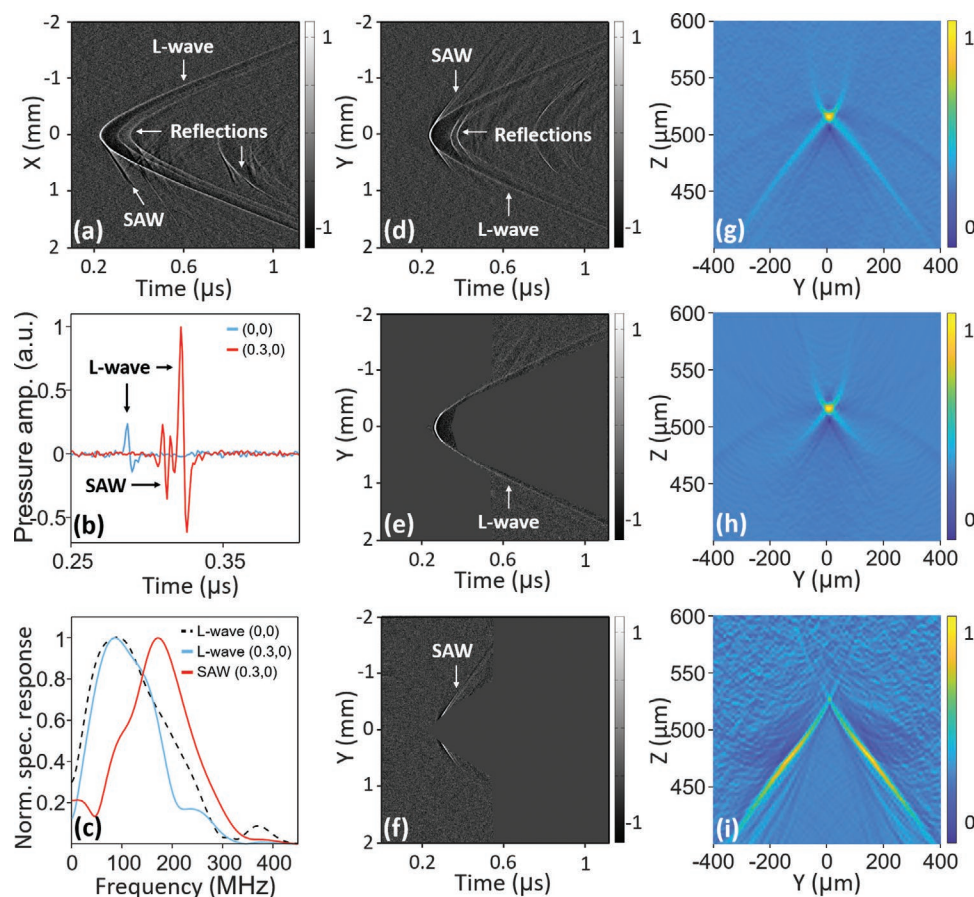


**Figure 2.** Frequency response and acoustic PSF of the SWED. a) Spatial response of the SWED acquired by linearly scanning over an acoustic point source in the  $x$ -direction as defined in Figure 1a. Grayscale color bar: normalized pressure amplitude. b) Temporal responses of the SWED at coordinates (0,0) and (0.3,0) in (a). L-waves, longitudinal ultrasonic waves; SAWs, surface acoustic waves. c) Acoustic spectrum of the signals in (b). L-waves detected at coordinates (0,0) and (0.3,0) – black-dashed and blue curves, respectively, and SAWs detected at coordinate (0.3,0) – red curve. d) Spatial response of the SWED acquired by linearly scanning over an acoustic point source in the  $y$ -direction as defined Figure 1a. e) Spatial response of the SWED in (d) with the SAWs manually removed. f) Spatial response of the SWED in (d) with the L-waves manually removed. g) Projection of the acoustic PSF along the  $yz$ -plane with contributions from both L-waves and SAWs. Color bar: normalized. h) Projection of the acoustic PSF along the  $yz$ -plane with contribution of L-waves only. i) Projection of the acoustic PSF along the  $yz$ -plane with contribution of SAWs only.

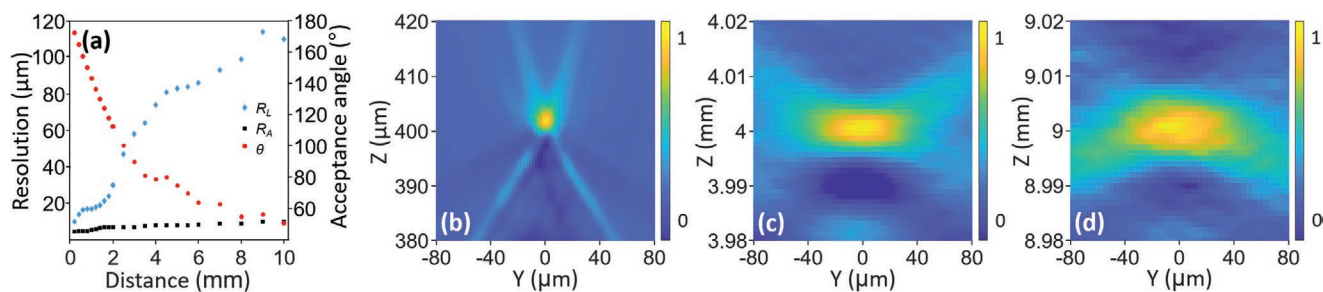
of L-waves in water. We also observed linear profiles that indicate SAW propagation on the surface of the chip (“SAW;” Figure 2a,d). SAW waves are excited when L-waves are incident on the silicon–water interface at Rayleigh critical angles ( $\theta_c$ ),<sup>[18]</sup> the shape of these profiles correspond to  $r(t) = v_s t + h \tan \theta_c$ . By fitting these profiles, we found that SAW propagate on the interface with velocities of  $\approx 4800$  and  $\approx 5000$  m s<sup>-1</sup> in the  $x$ -direction (Figure 2a) and  $\approx 5600$  m s<sup>-1</sup> in the  $y$ -direction (Figure 2d). In general, those velocities depend on the crystallographic orientation of the chip and are close to the numbers reported in previous studies.<sup>[18,19]</sup> Figure 2d shows that SAWs are excited symmetrically around the SWED, while Figure 2a shows excitation only from one side, this is because the silicon–water interface continues all along the scanning length in the  $y$ -direction, while in the  $x$ -direction, this interface exists only from one side of the sensor (Figure 3b). Acoustic reflections between the chip and the cover slip are also visible in the B-scans (“Reflections;” Figure 2a,d).

Figure 2b depicts the detected ultrasonic signals at coordinates (0,0) and (0.3,0), with the different shapes of L-wave and

SAW clearly visible. In addition, the L-wave at (0.3,0) is stronger by fourfold than the L-wave at (0,0) as a result of the Rayleigh dip – a drop in the reflection coefficient of L-waves around the critical angle.<sup>[20]</sup> The spectral contents of the L-waves and the SAW (Figure 2c) indicate that the SWED has a detection bandwidth of 230 MHz at  $-6$  dB around 90 MHz for the L-waves, and a detection bandwidth of 190 MHz at  $-6$  dB around 172 MHz for the SAW.

The projections of the PSF along the  $yz$ - and  $xz$ -planes, where  $z$  is the axis corresponding to the imaging depth, can be obtained by reconstructing the B-scans. Figure 2g depicts the projection of the PSF along the  $yz$ -plane, where the point source did not reconstruct perfectly and elongated diagonal artefacts are visible emanating from the point source toward the bottom of the image. In order to investigate the contribution of the L-waves and the SAWs to the formation of the PSF, we modified the B-scan in Figure 2d by manually removing either the SAWs (Figure 2e) or the L-waves (Figure 2f).

The PSF formed only by the L-waves (Figure 2h) shows a marked improvement, with the artefact almost completely



**Figure 3.** Acoustic PSF dependence on the distance from the SWED. a) Dependence of the lateral ( $R_L$ ) – blue points and axial ( $R_A$ ) – black points resolutions on the distance from the sensor. The effective acceptance angle of the sensor ( $\theta$ ) during each measurement is denoted by red points. b) Projection of the PSF along the  $yz$ -plane at a distance of  $400\ \mu\text{m}$ . c) Projection of the PSF along the  $yz$ -plane at a distance of  $4\ \text{mm}$ . d) Projection of the PSF along the  $yz$ -plane at a distance of  $9\ \text{mm}$ .

disappearing. The remaining artefacts are characteristic of raster-scan optoacoustic mesoscopy, and are the result of the limited-view imaging geometry that does not cover the full  $360^\circ$  around the object.<sup>[21]</sup> The PSF formed only by the SAW (Figure 2i) does not correctly report the location and the shape of the object and is responsible for the artefacts in Figure 2g.

To quantify the effect of imaging depth on the resolution, we measured the acoustic PSF at distances varying from  $200\ \mu\text{m}$  to  $10\ \text{mm}$ . B-scans were performed with the SWED along the  $y$ -axis with a scanning length varying from  $6$  to  $9.6\ \text{mm}$  ( $2\ \mu\text{m}$  step) over an acoustic broadband point source. At each coordinate, the ultrasonic signals were recorded as a function of time with  $100$  averages and a  $[2, 500]$  MHz band-pass filter. The projections of the PSF along the  $yz$ -plane were reconstructed from the B-scans without removal of the SAW.

Figure 3a depicts the lateral ( $R_L$ ) and axial ( $R_A$ ) resolutions calculated from the full width half maximums (FWHMs) of the PSFs imaged by the SWED, and the effective acceptance angle of the sensor ( $\theta$ ) at each distance. Because of technical constraints of the imaging system, the scanning length was limited which resulted in reduction of  $\theta$  with distance. For distances larger than  $1\ \text{mm}$ ,  $\theta$  was smaller than the maximum acceptance angle of  $148^\circ$  reported for the SWED.<sup>[11]</sup> As expected,  $R_L$  and  $R_A$  gradually deteriorate from  $10$  and  $4.5\ \mu\text{m}$ , respectively, at  $200\ \mu\text{m}$  distance to  $110$  and  $10\ \mu\text{m}$ , respectively, at  $10\ \text{mm}$  distance. In the lateral direction, both the frequency-dependent acoustic attenuation<sup>[22]</sup> and the reduction in the effective acceptance angle<sup>[23]</sup> are responsible for the deterioration of the resolution with distance. In the axial direction, those effects are much subtler and the resolution is defined largely by the bandwidth of the sensor.<sup>[24]</sup> Figure 3b–d depicts the projection of the acoustic PSF along the  $yz$ -plane at imaging distances of  $400\ \mu\text{m}$ ,  $4\ \text{mm}$ , and  $9\ \text{mm}$ , respectively. The reduction in resolution is clearly visible in both the axes.

#### 4. Optoacoustic Imaging

To evaluate the performance of the SWED for optoacoustic mesoscopy, we imaged several vasculature-mimicking phantoms at a distance of  $\approx 200\ \mu\text{m}$  from the sensor. The detected signals were averaged  $20$  times and a  $[2, 350]$  MHz band-pass filter was applied. For all the images, the SAWs were not removed and the images were reconstructed from all the signals detected by the SWED in each scan.

First, we imaged a phantom constructed from two parallel carbon fibers with diameters of  $6$ – $8\ \mu\text{m}$  and a  $30\ \mu\text{m}$  black polystyrene suture (Dafilon Polyamide, B. Braun Melsungen AG, Germany) placed diagonally across the fibers. The 3D rendering of the reconstructed  $1.1 \times 1.1\ \text{mm}^2$  field of view ( $10\ \mu\text{m}$  step) is depicted in Figure 4a and shows that the phantom is well resolved. We also performed two B-scans with a finer step of  $1\ \mu\text{m}$  along the diameter of one of the carbon fibers and the suture. The lateral and axial profiles obtained from the reconstructed B-scans are depicted in Figure 4c,d, respectively, and the diameters of these phantoms can be estimated from the FWHM of those profiles.

Next, we imaged a layer of gold hexagonal mesh (G400HH, SPI Supplies; West Chester, PA, USA) with a bar width of  $8\ \mu\text{m}$  and sub-micrometer layer thickness. The 3D rendering of the reconstructed  $0.4 \times 0.4\ \text{mm}^2$  field of view ( $5\ \mu\text{m}$  step) is depicted in Figure 4b and shows that the phantom is well resolved with no distortions to the mesh. The lateral and axial profiles of a bar are depicted in Figure 4e, and the thickness and width of the bar can be estimated from the FWHMs of those profiles.

In order to demonstrate the ability of the SWED to perform 3D optoacoustic mesoscopy, we imaged two phantoms composed of  $30\ \mu\text{m}$  sutures embedded in several milliliters of agar gel. The detected signals were averaged  $20$  times and a  $[2, 350]$  MHz band-pass filter was applied. For all the images, the SAWs were not removed and the images were reconstructed from all the signals detected by the SWED in each scan.

The first phantom was constructed from three  $10\ \text{mm}$  long sutures placed loosely in the agar in order to demonstrate the ability to image a continuous object traversing and curving over a large volume. The 3D rendering of the reconstructed  $5 \times 5 \times 1\ \text{mm}^3$  volume ( $20\ \mu\text{m}$  step) is depicted in Figure 5a and the maximum intensity projections along the  $xy$ - and  $xz$ -planes are depicted in Figure 5b,c, respectively.

The second phantom was constructed from short pieces of sutures of varying lengths randomly mixed in the agar in order to demonstrate the ability to image and resolve a dense 3D phantom. The 3D rendering of the reconstructed  $4 \times 4 \times 1.2\ \text{mm}^3$  volume ( $20\ \mu\text{m}$  step) is depicted in Figure 5d and the maximum intensity projections (with the field of view set tightly around the phantom) along the  $xy$ - and  $xz$ -planes are depicted in Figure 5e,f, respectively. For both phantoms, the sutures are well resolved over the whole imaging volume. Discontinuities appear at some deep situated sutures (the white

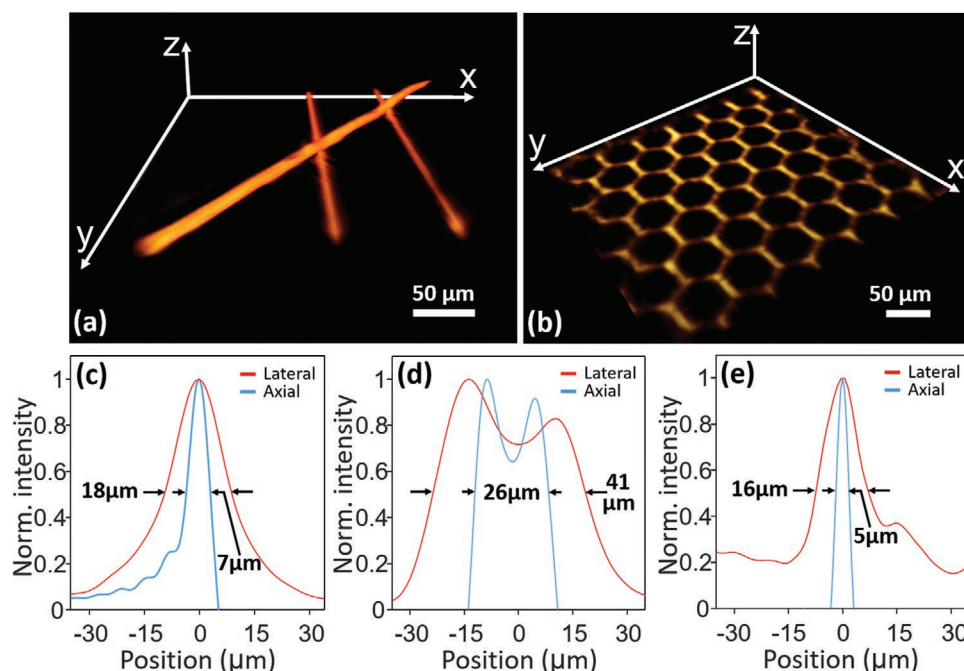


**Figure 4.** Epi-illumination optoacoustic mesoscopy of phantoms with the SWED. a) 3D rendering of a reconstructed  $1.1 \times 1.1 \text{ mm}^2$  field of view of a phantom composed of two parallel carbon fibers 6–8  $\mu\text{m}$  in diameter, and a 30  $\mu\text{m}$  polystyrene suture laying in diagonal, imaged with step of 10  $\mu\text{m}$ . b) 3D rendering of a reconstructed  $0.4 \times 0.4 \text{ mm}^2$  field of view of a thin layer of gold hexagonal grating with bar width of 8  $\mu\text{m}$  imaged with step of 5  $\mu\text{m}$ . c) Reconstructed profile of a carbon fiber imaged with a step of 1  $\mu\text{m}$ . d) Reconstructed profile of the suture imaged with a step of 1  $\mu\text{m}$ . e) Reconstructed profile of a bar from the hexagonal grating imaged with a step of 5  $\mu\text{m}$ .

arrows in Figure 5c,e). This is the result of nonhomogeneous illumination; as the phantom is illuminated from the top (epi-illumination) by only a single fiber, superficial sutures block the excitation laser, creating a shadow over deeper sutures. In addition, misalignments between the fiber and the SWED during

imaging result in asymmetrical illumination and only partial coverage of the SWED's acceptance angle, creating variations in width along the length of some sutures (Figure 5c,e). Both of the aforementioned effects are attributes of the imaging system rather than the sensor.

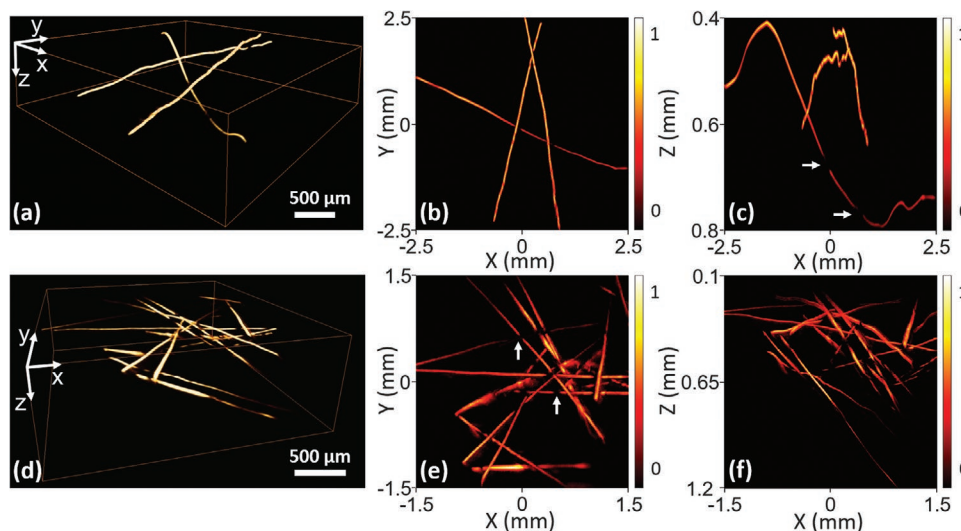


**Figure 5.** 3D rendering of phantoms imaged with the SWED. a) 3D rendering of a reconstructed  $5 \times 5 \times 1 \text{ mm}^3$  volume of a phantom composed of three 30  $\mu\text{m}$  polystyrene sutures imaged with step of 20  $\mu\text{m}$ . b) Maximum intensity projection of (a) along the  $xy$ -plane. c) Maximum intensity projection of (a) along the  $xz$ -plane. d) 3D rendering of a reconstructed  $4 \times 4 \times 1.2 \text{ mm}^3$  volume of a phantom composed of short 30  $\mu\text{m}$  polystyrene sutures randomly mixed in the agar, imaged with step of 20  $\mu\text{m}$ . e) Maximum intensity projection of (d) along the  $xy$ -plane. f) Maximum intensity projection of (d) along the  $xz$ -plane. The white arrows in the maximum intensity projection images point to examples of discontinuities in the sutures resulting from nonhomogeneous illumination.



## 5. Discussion

The results presented in Figure 2c indicate that the SWED responses to L-waves and SAWs are different. Detection of L-waves predominantly occurs in response to a change in the cavity length.<sup>[11]</sup> On the other hand, SAWs are a combination of longitudinal and transverse waves that propagate at the surface and interact with the SWED superficially, through the photoelastic effect and change of the cavity length. While the optical mode is well confined within the aperture of the SWED, along the Bragg grating, the optical field is centered around the discontinuity in the period but is not strictly confined to it.<sup>[25]</sup> The tighter light confinements along the aperture result in a smaller interaction volume, leading to a higher frequency response to the SAW.

Examination of the acoustic frequency response of the SWED to L-waves (Figure 2c) reveals that the dimensions of the SWED are 30-fold and 13-fold smaller than the cutoff wavelength of 230 MHz, satisfying the definition of a true point sensor when imaging with L-waves. Therefore, the expected resolution can be estimated by inserting the cutoff frequency ( $f_{\text{cut}}$ ), measured from the point source, and the definition for a point sensor ( $\varphi_a \approx 0$ ) into Equations (1) and (2). The expected isometric resolution of  $R_A \approx R_L \approx 5 \mu\text{m}$  was achieved only in the axial directions. The reconstructed suture and the carbon fiber did not experience any blurring in the axial direction and their diameters are close to the specified values (Figure 4c,d), as they are larger than the bandwidth-dependent axial resolution. By contrast, the sub-micrometer thickness of the reconstructed mesh in Figure 4b was smeared to  $5 \mu\text{m}$  (Figure 4e), which is the axial resolution limit of the SWED.

In the lateral direction, the reconstructed phantoms experienced a small amount of size-dependent blurring (Figure 4c–e). The diameters of the suture and carbon fiber and the width of the mesh bars are blurred by factors of  $\approx 1.4$ ,  $\approx 2.3$ , and  $\approx 2$ , respectively. The deviation of the phantom widths from the specifications (Figure 4c–e) can be attributed to insufficiently large field of view during imaging, resulting in an acceptance angle smaller than the maximum acceptance angle of the SWED,<sup>[23]</sup> and presence of SAW during image reconstruction. Reconstruction is performed assuming all the signals propagate at the speed of L-waves in water, and because SAWs propagate at higher velocities (Figure 2a,d), they do not sum coherently which results in artefacts that lead to lateral blurring (Figure 2g). In spite of that, the SAW-related blurring does not have a detrimental effect on the image quality, and it is possible to resolve fine features in dense phantoms over large imaging volumes imaged by the SWED (Figure 5).

The contribution of the artefacts to lateral blurring can be intuitively understood if we consider a 2D example of an object composed of adjacent point sources laying on the  $y$ -axis and tightly filling the interval  $[0, L]$  where  $L \gg \lambda_s$ . When the SWED performs a linear scan over that object at distance  $h$ , around the coordinate  $L/2$  (center of the object), the object would emit a plane-like acoustic wave with a wavefront that is parallel to the SWED aperture, therefore no SAWs would be excited. At this position in the reconstructed image, no artefacts would appear, and the thickness of the object can be precisely calculated from the emitted wavelength ( $\lambda_s$ ) if the cutoff frequency of the sensor

is  $f_{\text{cut}} > v_s/\lambda_s$ . When the SWED is located at coordinates that are smaller than 0 or larger than  $L$ , SAW can be excited because the edges of the object emit spherical-like waves. In the reconstructed image, the SAWs would introduce artefacts close to the edges of the objects, increasing the width of the object in the image. As the artefacts appear only at the edges, the larger the object, the smaller is the lateral blurring factor.

## 6. Conclusion

In this work, we demonstrated that the miniaturization and scalability offered by the silicon-photonics platform enable manufacturing of acoustic point sensors that offer superior image resolution, at any imaging depth, and superior integration density over what is possible to achieve using piezoelectric arrays or optical resonators manufactured from polymer. Previously, the subwavelength aperture of the SWED demonstrated super-resolution optoacoustic imaging only at shallow imaging depths ( $< \lambda_s$ ).<sup>[11]</sup> In this work, we experimentally demonstrate that the resolution achieved by the SWED surpasses the resolution achieved by any state-of-the-art sensor up to imaging depth of at least 10 mm, which has significant clinical relevance.

We acquired images with resolutions as small as  $16 \mu\text{m}$  laterally and  $5 \mu\text{m}$  axially – the best resolutions achieved in optoacoustic mesoscopy to date. The lateral resolution is degraded due to image artefacts originating from the presence of surface acoustic waves on the silicon–water interface. Nevertheless, the lateral and axial resolutions showcased herein are, respectively, twofold and sixfold better than what was demonstrated in optoacoustic mesoscopy and ultrasonic imaging with state-of-the-art focused piezoelectric sensors,<sup>[3]</sup> fivefold and 11-fold better than what was demonstrated with fiber-based plano-concave optical microresonator,<sup>[26]</sup> and 1.3-fold and threefold better than what was demonstrated with planar Fabry–Perot sensor.<sup>[24]</sup> The reported resolution could be improved by acquiring larger fields of view and characterizing the full acoustic PSF of the sensor and using it to correct the images.<sup>[27]</sup> The image quality demonstrated in this work can be further improved by upgrading the imaging system: employing several fibers for the delivery of the excitation laser and precise alignment of the sensor would result in homogenous illumination that covers all the acceptance angle of the SWED, ensuring that there are no dark regions in the imaging volume and the best possible resolution is achieved.

While purely optical modalities like microscopy and optical coherence tomography suffer from scattering that limits the imaging depth to few hundreds of micrometers and  $\approx 2$  mm, respectively, optoacoustic mesoscopy can reach depths of more than 10 times the transport mean free path,<sup>[28]</sup> which for most tissues would result in imaging depth larger than 10 mm. In this article, the sutures in the phantoms were spread over a depth of  $\approx 1.2$  mm (Figure 5), this imaging depth is not limited by the performance of the sensor. The imaging depth of optoacoustic mesoscopy can be limited by photon scattering that results in low optical fluence deep in the tissue and frequency-dependent acoustic attenuation. The first is more dominant, while the latter is responsible for the progressively deteriorating resolution deep in the tissue. In order to achieve optimal

imaging depth, it is possible to use homogenous illumination of 360° around the object, similar to multispectral optoacoustic tomography.<sup>[28]</sup>

In general, the sensitivity of optical resonators depends on the  $Q$ -factor, which in turn depends on the optical losses. Due to the enhanced bending losses, polymer MRRs under 20 μm result in  $Q$ -factors that are one order of magnitude smaller<sup>[7]</sup> than what is achieved by the SWED in this work. The typical propagation losses of the silicon-photonics platform set the maximum limit of the  $Q$ -factor to  $\approx 4 \times 10^5$ ,<sup>[29]</sup> and therefore the sensitivity of the SWED can be greatly improved by increasing the reflectivity of the Bragg grating through stronger corrugation.<sup>[30]</sup> It is also possible to increase the limit of the  $Q$ -factor by using the CMOS compatible low-loss rib waveguide design, as Bragg gratings based on rib waveguides were already successfully demonstrated.<sup>[31]</sup>

In order to reduce imaging time and avoid slow raster scanning, dense sensor arrays are required, with a pitch that is ideally smaller than half of the cutoff wavelength. MRR array was demonstrated with a very large pitch of  $\approx 90 \mu\text{m}$ <sup>[32]</sup> and this figure cannot be reduced without substantial loss of sensitivity. We demonstrated a SWED array with a pitch of 10 μm, which was an arbitrary choice that does not set the limit on the minimal value of the pitch. In silicon photonics, nonuniformities in the component density affect the etching plasma density and the performance of the components.<sup>[33]</sup> The SWED design offers higher density uniformity over the microring design, consequently the pitch can be safely reduced to a few micrometers. The uniformity of the density is also increased by the use of filler patterns (the rectangular mesh around the SWEDs in Figure 1d).

The SWED performance and resolution improvement reported in this work may have a substantial impact on the biomedical imaging field. For example, visualization of skin vasculature structure and angiogenesis are important hallmarks for conditions ranging from psoriasis<sup>[4]</sup> to melanoma.<sup>[34]</sup> While optical and optoacoustic microscopy modalities can be very attractive because they offer subcellular resolution, they are often unsuitable for monitoring the aforementioned hallmarks because imaging depth is limited to only few hundreds of micrometers, which is not appropriate for thickened psoriasis epidermis or deep tumors. With the SWED, optoacoustic mesoscopy is possible with lateral resolution < 20 μm up to a depth of 1.5 mm (Figure 3a). In addition, a resolution of at least 110 μm can be maintained up to depths of 10 mm, which surpasses the resolutions achieved by commercial piezoelectric linear arrays employed in medical ultrasound. The effect of the frequency-dependent acoustic attenuation at 10 mm can be estimated by calculating the effective  $f_{\text{cut}}$  from the measured axial resolution using Equation (1). At 10 mm,  $f_{\text{cut}}$  is reduced to 120 MHz, compared to 230 MHz at 0.53 mm. This  $f_{\text{cut}}$  is sufficient for imaging capillaries with diameters as small as 30 μm,<sup>[34]</sup> which is attractive for monitoring angiogenesis around deep tumors. Our sensor can simultaneously surpass the performance of the different sensors and sensing techniques employed in optoacoustic mesoscopy and medical ultrasound, indicating the possibility of easy combination of the two modalities in order to achieve complementary contrast for monitoring of tumor growth and metastasis. This ability alongside

the small size of the SWEDs is especially attractive for applications like endoscopic detection and grading of bladder cancer, where the tumor stage classifies the invasion depth into the bladder wall.<sup>[35]</sup> The SWED's high frequency response to surface acoustic waves could also be interesting for applications of bio- and chemical sensing.<sup>[36]</sup>

## Acknowledgements

The authors acknowledge financial support from the European Union's Horizon 2020 program under Grant Agreement No. 694968 (PREMSOT), and Grant Agreement No. 667933 (MIB) and from the Deutsche Forschungsgemeinschaft (DFG), Germany [Gottfried Wilhelm Leibniz Prize 2013; NT 3/10-1]. D.R. acknowledges financial support from Grant No. ERC-2015-CoG-682379. The authors thank Robert J. Wilson and Sergey Sulima for comments and discussion.

Open access funding enabled and organized by Projekt DEAL.

## Conflict of Interest

V.N. has financial interests in iThera Medical GmbH, Surgivision BV/ Bracco S.p.A, I3 Inc., and Spear UG.

## Data Availability Statement

The data that support the findings of this study are available from the corresponding author upon reasonable request.

## Keywords

microresonators, optical devices, optoacoustic imaging, optoacoustic materials, silicon photonics, ultrasound sensors, waveguides

Received: February 4, 2021

Revised: June 16, 2021

Published online: July 16, 2021

- [1] G. Wissmeyer, M. A. Pleitez, A. Rosenthal, V. Ntziachristos, *Light: Sci. Appl.* **2018**, *7*, 53.
- [2] M. Xu, L. V. Wang, *Phys. Rev. E: Stat. Phys., Plasmas, Fluids, Relat. Interdiscip. Top.* **2003**, *67*, 15.
- [3] M. Omar, J. Aguirre, V. Ntziachristos, *Nat. Biomed. Eng.* **2019**, *3*, 354.
- [4] J. Aguirre, M. Schwarz, N. Garzorz, M. Omar, A. Buehler, K. Eyerich, V. Ntziachristos, *Nat. Biomed. Eng.* **2017**, *1*, 0068.
- [5] X. L. Deán-Ben, I. Weidenfeld, O. Degtyaruk, V. Ntziachristos, A. C. Stiel, D. Razansky, *Neoplasia* **2020**, *22*, 441.
- [6] M. Omar, D. Soliman, J. Gateau, V. Ntziachristos, *Opt. Lett.* **2014**, *39*, 3911.
- [7] C. Zhang, S. L. Chen, T. Ling, L. J. Guo, *IEEE Sens. J.* **2015**, *15*, 3241.
- [8] B. Dong, H. Li, Z. Zhang, K. Zhang, S. Chen, C. Sun, H. F. Zhang, *Optica* **2015**, *2*, 169.
- [9] B. Dong, S. Chen, Z. Zhang, C. Sun, H. F. Zhang, *Opt. Lett.* **2014**, *39*, 4372.
- [10] P. Morris, A. Hurrell, A. Shaw, E. Zhang, P. Beard, *J. Acoust. Soc. Am.* **2009**, *125*, 3611.
- [11] R. Shnaiderman, G. Wissmeyer, O. Ülgen, Q. Mustafa, A. Chmyrov, V. Ntziachristos, *Nature* **2020**, *585*, 372.



- [12] X. Chen, M. M. Milosevic, S. Stanković, S. Reynolds, T. D. Bucio, K. Li, D. J. Thomson, F. Gardes, G. T. Reed, *Proc. IEEE* **2018**, *106*, 2101.
- [13] A. P. Jathoul, J. Laufer, O. Ogunlade, B. Treeby, B. Cox, E. Zhang, P. Johnson, A. R. Pizzey, B. Philip, T. Marafioti, M. F. Lythgoe, R. B. Pedley, M. A. Pule, P. Beard, *Nat. Photonics* **2015**, *9*, 239.
- [14] K. Haedicke, L. Agemy, M. Omar, A. Berezhnoi, S. Roberts, C. Longo-Machado, M. Skubal, K. Nagar, H. Hsu, K. Kim, T. Reiner, J. Coleman, V. Ntziachristos, A. Scherz, J. Grimm, *Nat. Biomed. Eng.* **2020**, *4*, 286.
- [15] F. Van Laere, W. Bogaerts, D. Taillaert, P. Dumon, D. Van Thourhout, R. Baets, in *OFC/NFOEC 2007 – Optical Fiber Communication and the National Fiber Optic Engineers Conf.*, IEEE, Piscataway, NJ **2007**, <https://doi.org/10.1109/OFC.2007.4348869>.
- [16] P. K. Köstl, F. Martin, B. Hans, W. P. Heinz, *Phys. Med. Biol.* **2001**, *46*, 1863.
- [17] E. M. Strohm, E. S. L. Berndl, M. C. Kolios, *Photoacoustics* **2013**, *1*, 49.
- [18] G. M. Crean, A. Waintal, *J. Appl. Crystallogr.* **1986**, *19*, 181.
- [19] T. Tachizaki, T. Muroya, O. Matsuda, Y. Sugawara, D. H. Hurley, O. B. Wright, *Rev. Sci. Instrum.* **2006**, *77*, 043713.
- [20] J. D. N. Cheeke, *Fundamentals and Applications of Ultrasonic Waves Fundamentals and Applications of Ultrasonic Waves*, CRC Press, Boca Raton, FL **2002**.
- [21] A. Rosenthal, V. Ntziachristos, D. Razansky, *Curr. Med. Imaging Rev.* **2013**, *9*, 318.
- [22] X. L. Deán-Ben, D. Razansky, V. Ntziachristos, *Phys. Med. Biol.* **2011**, *56*, 6129.
- [23] Y. Xu, D. Feng, L. V. Wang, *IEEE Trans. Med. Imaging* **2002**, *21*, 823.
- [24] E. Zhang, J. Laufer, P. Beard, *Appl. Opt.* **2008**, *47*, 561.
- [25] T. Liu, M. Han, *IEEE Sens. J.* **2012**, *12*, 2368.
- [26] J. A. Guggenheim, J. Li, T. J. Allen, R. J. Colchester, S. Noimark, O. Ogunlade, I. P. Parkin, I. Papakonstantinou, A. E. Desjardins, E. Z. Zhang, P. C. Beard, *Nat. Photonics* **2017**, *11*, 714.
- [27] M. Omar, J. Rebling, K. Wicker, T. Schmitt-Manderbach, M. Schwarz, J. Gateau, H. López-Schier, T. Mappes, V. Ntziachristos, *Light: Sci. Appl.* **2017**, *6*, e16186.
- [28] V. Ntziachristos, *Nat. Methods* **2010**, *7*, 603.
- [29] J. Niehusmann, A. Vörckel, P. H. Bolivar, T. Wahlbrink, W. Henschel, H. Kurz, *Opt. Lett.* **2004**, *29*, 2861.
- [30] Y. Painchaud, M. Poulin, C. Latrasse, N. Ayotte, M.-J. Picard, M. Morin, in *Advanced Photonics Congress*, OSA Technical Digest (online), OSA, Colorado Springs, Colorado, USA **2012**, p. BW2E.3.
- [31] X. Wang, W. Shi, H. Yun, S. Grist, N. a. F. Jaeger, L. Chrostowski, *Opt. Express* **2012**, *20*, 15547.
- [32] A. Maxwell, S. W. Huang, T. Ling, J. S. Kim, S. Ashkenazi, L. J. Guo, *IEEE J. Sel. Top. Quantum Electron.* **2008**, *14*, 191.
- [33] W. Bogaerts, L. Chrostowski, *Laser Photonics Rev.* **2018**, *12*, 1700237.
- [34] M. Omar, M. Schwarz, D. Soliman, P. Symvoulidis, V. Ntziachristos, *Neoplasia* **2015**, *17*, 208.
- [35] F. Placzek, E. C. Bautista, S. Kretschmer, L. M. Wurster, F. Knorr, G. González-Cerdas, M. T. Erkkilä, P. Stein, Ç. Ataman, G. G. Hermann, K. Mogensen, T. Hasselager, P. E. Andersen, H. Zappe, J. Popp, W. Drexler, R. A. Leitgeb, I. W. Schie, *Analyst* **2020**, *145*, 1445.
- [36] Y. Wang, Z. Xu, Y. Wang, J. Xie, *Sensors* **2017**, *17*, 1813.